ARTICLE

A New Free-Standing Aqueous Zinc-Ion Capacitor Based on MnO$_2$–CNTs Cathode and MXene Anode

Siliang Wang[1,2], Qiang Wang[1,2], Wei Zeng[1,2] ✉, Min Wang[1,2], Limin Ruan[1,2], Yanan Ma[3] ✉

✉ Wei Zeng, youfmail@163.com; Yanan Ma, mayn@huat.edu.cn

[1] Key Laboratory of Intelligent Computing and Signal Processing, Ministry of Education, Anhui University, No. 3 Feixi Road, Hefei 230039, Anhui Province, People's Republic of China

[2] National Engineering Research Center for Agro-Ecological Big Data Analysis and Application, School of Electronics and Information Engineering, Anhui University, No. 111 Jiulong Road, Hefei 230601, Anhui Province, People's Republic of China

[3] School of Sciences, Hubei University of Automotive Technology, No. 167 Checheng West Road, Shiyan 442002, Hubei Province, People's Republic of China

HIGHLIGHTS

- A new zinc-ion capacitor (ZIC) was realized by assembling the free-standing manganese dioxide–carbon nanotubes (MnO$_2$–CNTs) battery-type cathode and MXene (Ti$_3$C$_2$T$_x$) capacitor-type anode in an aqueous electrolyte.

- The large specific capacitance of the MXene anode avoids the mismatch in capacitance between the cathode and anode of the ZIC.

- The superior performance of the proposed ZIC makes it a promising candidate for the next-generation energy storage devices.

ABSTRACT Restricted by their energy storage mechanism, current energy storage devices have certain drawbacks, such as low power density for batteries and low energy density for supercapacitors. Fortunately, the nearest ion capacitors, such as lithium-ion and sodium-ion capacitors containing battery-type and capacitor-type electrodes, may allow achieving both high energy and power densities. For the inspiration, a new zinc-ion capacitor (ZIC) has been designed and realized by assembling the free-standing manganese dioxide–carbon nanotubes (MnO$_2$–CNTs) battery-type cathode and MXene (Ti$_3$C$_2$T$_x$) capacitor-type anode in an aqueous electrolyte. The ZIC can avoid the insecurity issues that frequently occurred in lithium-ion and sodium-ion capacitors in organic electrolytes. As expected, the ZIC in an aqueous liquid electrolyte exhibits excellent electrochemical performance (based on

the total weight of cathode and anode), such as a high specific capacitance of 115.1 F g^{-1} (1 mV s^{-1}), high energy density of 98.6 Wh kg^{-1} (77.5 W kg^{-1}), high power density of 2480.6 W kg^{-1} (29.7 Wh kg^{-1}), and high capacitance retention of ∼ 83.6% of its initial capacitance (15,000 cycles). Even in an aqueous gel electrolyte, the ZIC also exhibits excellent performance. This work provides an essential strategy for designing next-generation high-performance energy storage devices.

KEYWORDS Energy storage; Zinc-ion capacitor; Battery-type and capacitor-type electrodes; MXene; Electrochemical performance
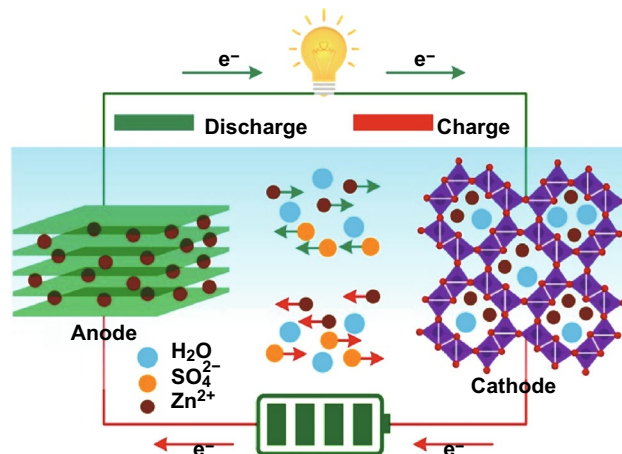
1 Introduction

The issues of energy depletion and greenhouse effect owing to the over-consumption of non-renewable resources urgently require alternative green energy and efficient energy storage devices [1–3]. Currently, batteries (e.g., lithium-ion batteries, alkaline zinc–manganese batteries, and lead–acid batteries) and supercapacitors are the main energy storage devices [4–7]. Owing to their clear advantages (e.g., higher power density, longer cycle life, better cycle stability, and higher safety), supercapacitors are more promising energy storage devices compared with batteries [8–10]. However, restricted by their energy storage mechanisms, supercapacitors possess low energy density [11, 12]. To improve energy density without sacrificing the power density of supercapacitors, constructing ion capacitors, such as lithium-ion or sodium-ion capacitors, is possible. In the ion capacitors, battery-type electrodes and capacitor-type electrodes are paired in electrolytes [13–18]. For example, in the lithium-ion capacitor, the lithium-ion battery-type anode (cathode) contributes a high capacity using the lithium-ion insertion/extraction reaction, while the capacitor-type cathode (anode) provides high power by rapid ion adsorption/desorption. Therefore, lithium-ion capacitors possess higher energy density than supercapacitors and higher power density than batteries [16, 17]. Although considerable progress has been made in the area of lithium-ion and sodium-ion capacitors, the following drawbacks severely restrict their practical application [14, 15]. First, most lithium-ion and sodium-ion capacitors contain organic electrolytes that are flammable, volatile, and toxic. Second, the kinetics and capacitance mismatch owing to the sluggish kinetics of lithium-ion and sodium-ion battery-type electrodes and low specific capacitance of capacitor-type electrodes in organic electrolytes bring huge difficulties in implementing high-performance devices. Finally, determined by the intrinsic properties of lithium-ion and sodium-ion battery-type electrodes, the cycle life of these ion capacitors remains low. Therefore, employing new ion capacitor containing aqueous electrolytes that are safe and have long cycle life is essential.

Currently, rechargeable aqueous zinc-ion batteries have attracted considerable attention for their high capacity, fast kinetics, and high safety [19–22]. These unique properties of zinc-ion batteries give us an inspiration for designing novel zinc-ion capacitors (ZIC) that is composed of zinc-ion insertion/extraction battery-type cathodes and suitable capacitor-type anodes. Many materials (e.g., such as manganese-based oxides, vanadium-based oxides, Prussian blue analogs, Chevrel phase compounds, and polyanion compounds) have been used as the cathodes in zinc-ion batteries [23, 24]. Among these materials, manganese-based oxides, such as manganese dioxide (MnO_2), have unique advantages of natural abundance, low toxicity, low cost, and multiple valence states of Mn [20, 21], which makes them potential battery-type cathode materials for ZIC.

Activated carbon (AC) is commonly used for a capacitor-type electrode in lithium-ion and sodium-ion capacitors [16, 25, 26]. However, using AC for capacitor-type electrode has following two defects: (1) AC-based electrodes exhibit limited capacity owing to the energy storage mechanism of electrochemical double-layer capacitors. (2) AC-based electrodes require the binder and conductive-additive, which increases the weight of the electrodes and decreases the final specific capacitance of the devices. Therefore, AC is unsuitable for the high-performance ZIC. MXene, a new type of two-dimensional (2D) layered materials with the formula of $M_{n+1}X_nT_x$ (M represents the early transition metal, X represents carbon or nitrogen, and T_x represents F, O, and OH surface termination, $n = 1, 2, 3$), is extensively used in the field of energy storage owing to its superior properties of high conductivity, hydrophilic surface, and energy storage mechanism of intercalation/de-intercalation pseudo-capacitance [27–29]. Based on the properties and applications of MXene, we believe that MXene is a suitable capacitor-type electrode material for the ZIC.

Herein, we designed and realized an aqueous ZIC based on free-standing manganese dioxide–carbon nanotubes (MnO_2–CNTs) battery-type cathode and $Ti_3C_2T_x$ (as a representative of the MXene family) capacitor-type anode. In summary, the aqueous ZIC has the following advantages compared with the state-of-the-art lithium-ion and sodium-ion capacitors based on organic electrolytes: (1) The use of aqueous liquid or gel electrolytes does not pose any serious safety issues. (2) The use of MXene capacitor-type anode (intercalation/de-intercalation energy storage mechanism) eliminates the above-mentioned mismatch in kinetics and capacitance. (3) Compared with organic electrolytes, aqueous electrolytes are more stable during the charge–discharge cycles, which contribute to the long cycle life of the ZIC. As a proof of concept, the ZIC in an aqueous liquid electrolyte exhibits a high specific capacitance of 115.1 F g^{-1} (scan

rate of 1 mV s^{-1}), a high energy density of 98.6 Wh kg^{-1} (power density of 77.5 W kg^{-1}), a high power density of 2480.6 W kg^{-1} (energy density of 29.7 Wh kg^{-1}), a high capacitance retention of ~ 83.6% of its initial capacitance after 15,000 cycles, and a high Coulombic efficiency of above 93.3% during the cycles. Even in an aqueous gel electrolyte, the ZIC also exhibits an excellent performance. This study provides an effective way to design next-generation energy storage devices exhibiting high energy and power densities, excellent cycle stability, long life, and high safety.

2 Experimental Section

2.1 Reagents and Materials

Carbon nanotubes (CNTs, multi-walled, diameter ≤ 8 nm, length = 0.5–2 μm) were purchased from Beijing Boyu Gaoke New Material Technology Co., Ltd. Manganese acetate tetrahydrate [Mn(CH$_3$COO)$_2$·4H$_2$O], ammonium persulfate [(NH$_4$)$_2$S$_2$O$_8$], 1-octanol, manganese sulfate monohydrate (MnSO$_4$·H$_2$O), hydrochloric acid (HCl), sodium dodecylbenzenesulfonate (SDBS), gelatin, and borax were purchased from Sinopharm Chemical Reagent Co., Ltd. Lithium fluoride (LiF) and zinc sulfate heptahydrate (ZnSO$_4$·7H$_2$O) were purchased from Aladdin Industrial Corporation and Sahn Chemical Technology (Shanghai) Co., Ltd., respectively.

2.2 Fabrication of Free-Standing MnO$_2$–CNTs Electrodes

MnO$_2$ nanowires (NWs) were prepared by a method similar to our previous work [30]. CNTs, MnO$_2$ NWs, and SDBS with appropriate weight ratios were mixed and put into deionized water (30 mL). The mixture was probe ultrasonicated for 30 min to form a homogeneous suspended solution. The prepared suspended solution was filtered through a membrane (pore size of 450 nm). After the filtered cake was dried and peeled off, a free-standing MnO$_2$–CNTs electrode was obtained.

2.3 Fabrication of Free-Standing MXene Electrodes

The MXene (Ti$_3$C$_2$T$_x$) nanosheets were prepared according to our previous work [31, 32]. Briefly, LiF (1 g) was

added to HCl (9 M, 20 mL), followed by magnetic stirring until LiF completely dissolved. Ti$_3$AlC$_2$ (1 g) was gently added to the above solution and magnetically stirred for 24 h (35 °C). After etching, the mixture was centrifuged several times. After centrifugation, the precipitate was re-dispersed in deionized water and sonicated for 1 h (Ar atmosphere below 35 °C) followed by centrifugation. Finally, the dark green supernatant of MXene nanosheets was achieved. The free-standing MXene electrodes were fabricated by directly filtering the MXene solution through a membrane (pore size of 450 nm) followed by drying and peeling off the filtered cake of MXene.

2.4 Fabrication of Aqueous Liquid and Aqueous Gel Electrolytes

To prepare the aqueous liquid electrolyte, ZnSO$_4$·7H$_2$O (23 g) and MnSO$_4$·H$_2$O (0.676 g) were dissolved in deionized water (29.8 mL) and stirred until the solution was clarified. To prepare the aqueous gel electrolyte, gelatin (4.0 g) and borax (0.4 g) were added to deionized water (29.8 mL) and continuously magnetically stirred at 80 °C. After gelatin completely dissolved, ZnSO$_4$·7H$_2$O (23 g) and MnSO$_4$·H$_2$O (0.676 g) were added to the solution, and the stirring continued until a homogeneous solution was formed.

2.5 Assembling the ZIC

The free-standing MnO$_2$–CNTs and MXene films were cut to suitable sizes. The aqueous liquid ZIC was prepared by assembling the free-standing MnO$_2$–CNTs cathode (pre-activated at a current density of 0.256 A g^{-1} for three charge–discharge cycles) and MXene anode with a liquid electrolyte-soaked (2 M ZnSO$_4$ and 0.1 M MnSO$_4$) separator in between. After changing the liquid electrolyte to gel electrolyte, the quasi-solid ZIC was prepared by the fabrication process similar to that for the aqueous liquid ZIC.

2.6 Characterization

The morphology, structure, and composition of the samples were investigated using scanning electron microscopy (SEM, S-4800), transmission electron microscopy (TEM, JEM-2100), and X-ray diffraction (XRD, SmartLab, 9 KW). The electrochemical performances of the MnO$_2$–CNTs

cathode and MXene anode, such as cyclic voltammograms (CV), galvanostatic charge–discharge (GCD), and electrochemical impedance spectrum (EIS), were conducted on an electrochemical workstation (CHI660E) using metallic zinc foils as a counter-electrode and 2 M $ZnSO_4$ and 0.1 M $MnSO_4$ as an electrolyte in an electrolytic cell. The electrochemical performances of the ZIC in aqueous liquid and gel electrolyte were tested using a two-electrode system. The mass ratio of the MnO_2–CNTs cathode to MXene anode was 1:2.14 according to the charge balance between the cathode and anode.

3 Results and Discussion

The schematic diagram of the ZIC is shown in Fig. 1a. The ZIC consists of a MnO_2–CNTs battery-type cathode (pre-activated by charge–discharge cycles), MXene capacitor-type anode, and 2 M $ZnSO_4$ and 0.1 M $MnSO_4$ electrolyte. In the steady state, the energy storage mechanism of the ZIC can be described briefly as follows. During charging, the zinc ions are extracted from the tunnels of MnO_2 into electrolyte and subsequently intercalate into the interlayer of MXene. During discharging, the zinc ions de-intercalate from MXene into electrolyte and subsequently insert into the tunnels of MnO_2. Both battery-type and capacitor-type energy storage mechanisms such as zinc-ion insertion/extraction (MnO_2) and intercalation/de-intercalation (MXene) result in high energy and power densities of the

ZIC. $MnSO_4$ with an appropriate concentration was added to effectively inhibit the dissolution of MnO_2, which significantly improved the cycle life of the ZIC. Figure 1b shows the fabrication procedure of the free-standing MnO_2–CNTs cathode and MXene anode. To prepare the MnO_2–CNTs electrode, MnO_2 nanowires (NWs) and CNTs were probe sonicated for 30 min. Then, the well-mixed solution was vacuum-filtered through a membrane followed by vacuum drying. Finally, free-standing MnO_2–CNTs film was peeled off from the membrane. A similar method was adopted to prepare a free-standing MXene electrode. Because the MXene solution with high dispersion can be obtained by liquid exfoliation, the solution was directly vacuum-filtered and did not require the step of probe sonication.

To prepare the free-standing MnO_2–CNTs electrodes, MnO_2 NWs need to be synthesized. Figure 2a shows the SEM image of MnO_2, which shows the entangled MnO_2 NWs. The TEM image of MnO_2 NWs is shown in Fig. 2b. In the TEM image, the lattice fringes can be clearly observed, which illustrates the high crystallization of MnO_2 NWs. The MnO_2 NWs have a diameter of 5–25 nm and length of 0.2–2 μm (Fig. S1a). The elemental mapping images of the MnO_2 NWs (Fig. S1b) clearly show Mn and O. The XRD pattern of the MnO_2 NWs (Fig. 2c) further confirms that MnO_2 belongs to the tetragonal α-MnO_2 phase (JCPDS No. 44-0141) [30, 33]. Before preparing the free-standing MXene electrodes, the highly dispersed MXene solution needs to be obtained. Figure S2 shows the Tyndall scattering effect of the MXene colloid, which illustrates the excellent
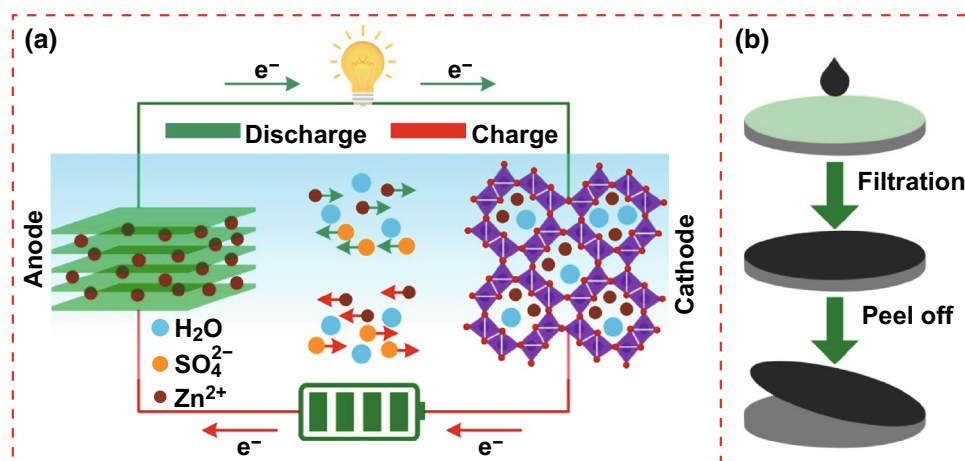
Fig. 1 Schematic diagram of the ZIC and fabrication procedure of the free-standing electrodes, **a** schematic diagram of the ZIC: MnO_2–CNTs serve as the cathode, MXene serves as the anode, and 2 M $ZnSO_4$ and 0.1 M $MnSO_4$ serve as the electrolyte; **b** fabrication procedure of the free-standing MnO_2–CNTs cathode and MXene anode
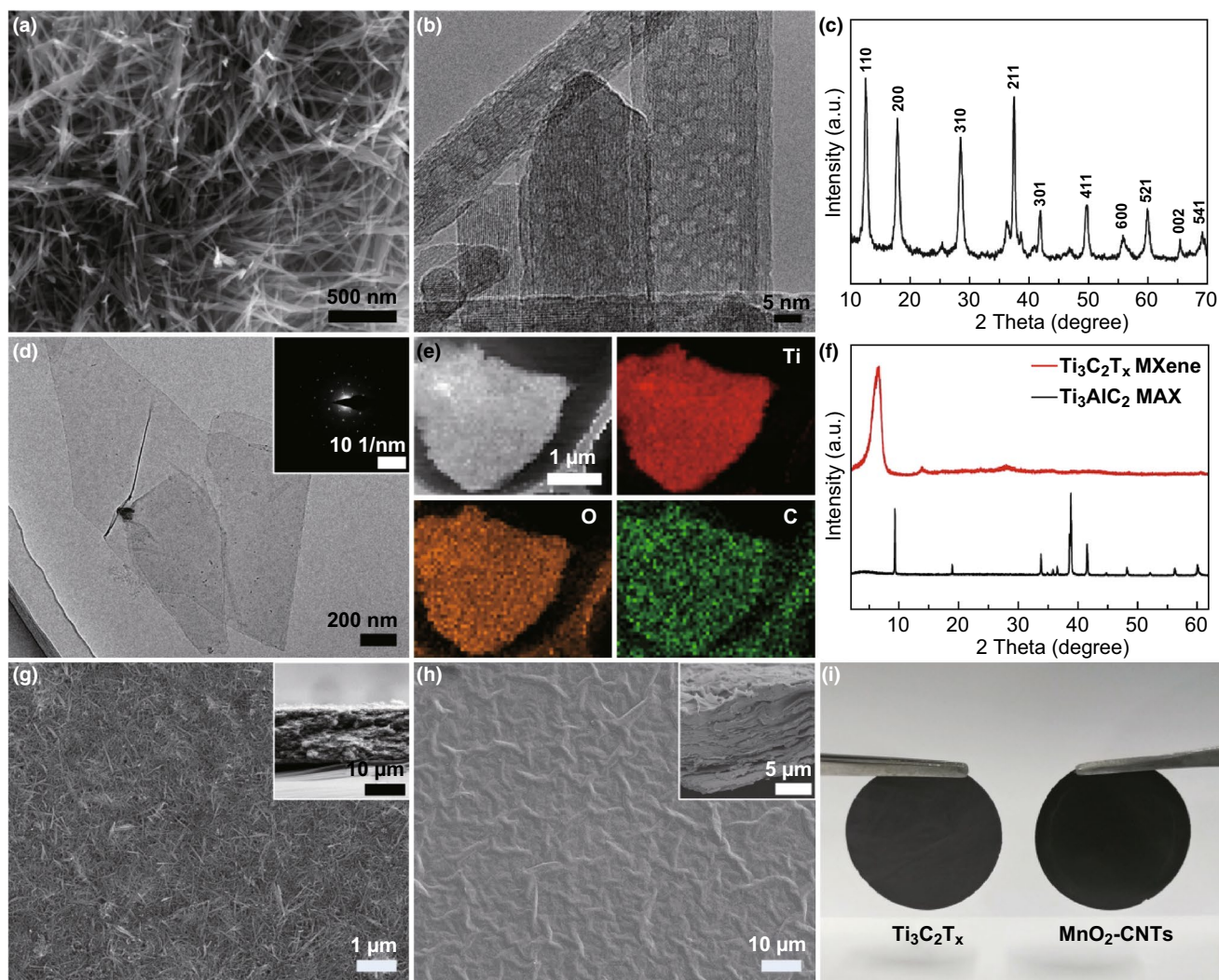
Fig. 2 Characterization of the MnO_2–CNTs battery-type cathode and MXene capacitor-type anode. **a** SEM image, **b** HRTEM image, and **c** XRD pattern of the MnO_2 NWs. **d** TEM image of the MXene nanosheets, inset is the corresponding SAED, **e** elemental mapping images of the MXene nanosheets, and **f** XRD patterns of MAX and MXene. SEM images of **g** MnO_2–CNTs and **h** MXene electrodes, insets are the corresponding cross-sectional SEM images, respectively. **i** Photographs of the free-standing MnO_2–CNTs and MXene electrodes

dispersion of the MXene nanosheets. The two-dimensional lamellar structure of MXene is shown in the TEM image in Fig. 2d. Figure 2d inset shows the selected area electron diffraction (SAED) of the MXene nanosheets, exhibiting a typical hexagonal symmetry diffraction pattern, which demonstrates the single-crystal structure of the MXene nanosheets. Ti, C, and O in $Ti_3C_2T_x$ MXene are clearly observed in the elemental mapping images in Fig. 2e. XRD was conducted to further illustrate the successful preparation of MXene. As shown in Fig. 2f, after etching Al from Ti_3AlC_2 MAX, the typical peaks of Ti_3AlC_2 MAX disappear, and a new peak at approximately 7°, which belongs to $Ti_3C_2T_x$ MXene,

appears [34]. Figure 2g and the inset show the surface and cross-sectional SEM images of the MnO_2–CNTs cathode, respectively. The thickness of the MnO_2–CNTs cathode is approximately 12.5 μm. The MnO_2 NWs are dispersed uniformly in CNTs, which is beneficial for charge transport. The wrinkled structure of the MXene anode with a thickness of approximately 11.5 μm (Fig. 2h inset) is shown in the surface SEM images (Fig. 2h). Figure 2i presents the photographs of the free-standing MnO_2–CNTs cathode and MXene anode.

The typical two-electrode system was used in electrochemical measurements to evaluate the electrochemical

performance of the MnO$_2$–CNTs electrodes. Figures 3a and S3a–c show the GCD curves of the MnO$_2$–CNTs electrodes with different weight ratios. All GCD curves present the clear charge–discharge voltage plateaus. The corresponding relation between the specific capacity and current density of the MnO$_2$–CNTs electrodes can be seen in Fig. 3b. When the current density is 0.256 A g^{-1}, the specific capacity of the MnO$_2$–CNTs electrode with the CNTs to MnO$_2$ weight ratio of 4/3 is as high as 254.1 mAh g^{-1}, which is much larger than those in previous reports [35–37]. Compared with the other weight ratios, the MnO$_2$–CNTs electrode with the CNTs to MnO$_2$ weight ratio of 4/3 exhibits the largest specific capacity at the same current density (Fig. S4).

This observation can be explained as follows. Because the MnO$_2$ has higher theoretical capacity than CNTs, when the content of MnO$_2$ in the MnO$_2$–CNTs electrode is increased, the corresponding specific capacity is improved. However, the excessive content of MnO$_2$ leads to the reduced specific capacity for the intrinsically poor electrical conductivity of MnO$_2$. Therefore, there is an optimum CNT to MnO$_2$ weight ratio. This phenomenon has been also observed in other studies [38, 39]. Based on the above results and analyses, the MnO$_2$–CNTs electrode with a weight ratio of 4/3 was chosen for the cathode of ZIC. To better understand the excellent performance of the MnO$_2$–CNTs cathode, electrochemical kinetics was studied in detail based on the CV curves at
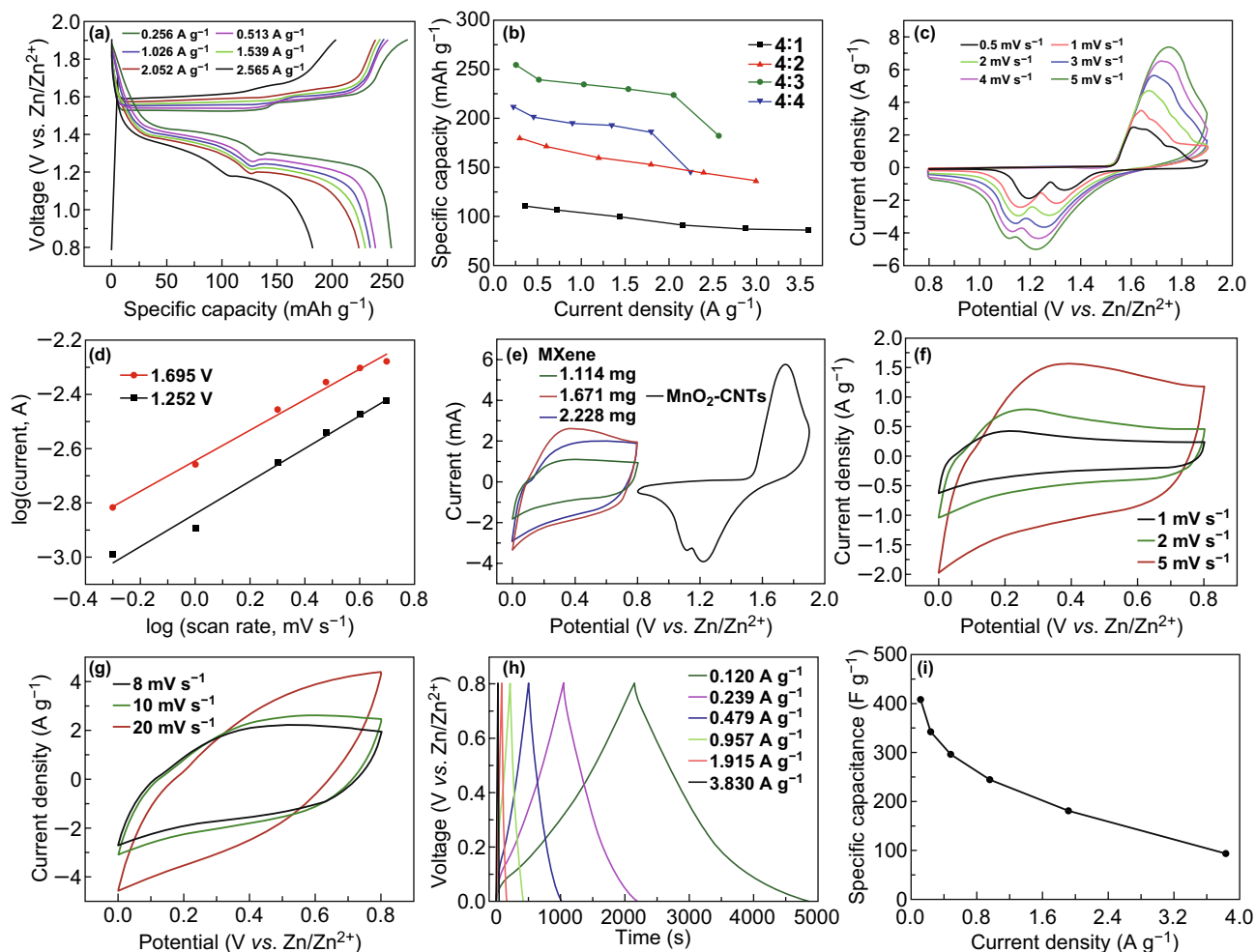
Fig. 3 Electrochemical performance of the MnO$_2$–CNTs and MXene electrodes. **a** GCD curves with various current densities of the optimum MnO$_2$–CNTs electrode. **b** Specific capacitance versus current density of the MnO$_2$–CNTs electrodes with various CNTs to MnO$_2$ weight ratios. **c** CV curves with various scan rates of the optimum MnO$_2$–CNTs electrode. **d** log (i) versus log (v) plots of the current response at the voltages of 1.695 V and 1.252 V. **e** CV curves of the MXene electrodes (various mass loadings) and MnO$_2$–CNTs cathode at a scan rate of 5 mV s^{-1}. **f, g** CV curves with various scan rates, **h** GCD curves with various current densities, and **i** specific capacitance versus current density of the MXene anode

various scan rates (Fig. 3c). Based on the power law, the relation between the measured current (i) and scan rates (v) obeys an empirical relation: $i = av^b$, where a and b are the adjustable parameters. From the slope of the log (i) versus log (v) plot, the value of b providing insight into the energy storage mechanism can be obtained. The value of b close to 0.5 means a diffusion-controlled process, while the value of b near 1 indicates that the electrochemical reaction is dominated by the surface capacitive-controlled process [40]. Figure 3d shows that the b values at 1.252 and 1.695 V are 0.60 and 0.56, respectively. These values imply that the corresponding reaction in the MnO_2–CNTs cathode is mainly controlled by ion diffusion.

It is known that the capacitance balance between the cathode and anode is extremely important to maximize the energy density of the ion capacitors [41, 42]. Thus, the MXene free-standing electrodes with various mass loadings were prepared. Figure 3e shows the CV curves of the MXene electrodes and MnO_2–CNTs cathode. The capacitance of the MXene electrode with a mass loading of 1.671 mg (0.7 cm^2) is closest to that of the MnO_2–CNTs cathode at a scan rate of 5 mV s^{-1}. Thus, MXene electrode with this mass loading was used as the anode of ZIC. Next, CV and GCD were investigated to characterize the electrochemical performance of the MXene anode. Figure 3f, g presents the CV curves of the MXene anode. As expected, the CV plots show the rectangular curves, which indicate the ideal capacitive behavior of the anode. The GCD curves in Fig. 3h exhibit good linear potential–time profiles, which further demonstrate the excellent electrochemical performance of the anode. The specific capacitance of the MXene anode evaluated by the above GCD results can be seen in Fig. 3i. The specific capacitance decreases with the increase in current density. When the current density is 0.12 A g^{-1}, the specific capacitance of the anode is as high as 408 F g^{-1}. The large specific capacitance of the anode avoids the mismatch in capacitance between the cathode and anode of the ZIC.

As a proof of concept, the electrochemical performance of the ZIC in an aqueous liquid electrolyte based on the free-standing MnO_2–CNTs cathode and MXene anode was investigated. Figure 4a, b shows the CV curves of the ZIC with scan rates from 1 to 20 mV s^{-1}. The CV curves exhibit typical redox peaks and large current densities. In Fig. 4c, the well-symmetric GCD curves (current densities from 0.082 to 2.611 A g^{-1}) are observed, which further demonstrate the good electrochemical performance of the ZIC. Based on the

above CV results, the relation between specific capacitance of the ZIC and scan rate is shown in Fig. 4d. With the scan rate increases from 1 to 20 mV s^{-1}, the specific capacitance of the ZIC decreases from 115.1 to 67.5 F g^{-1}. Because the GCD curves are approximately linear (Fig. 4c), the power density (P) and energy density (E) of the ZIC are calculated using the following relation: $P = (V_{max} + V_{min})i/2m$, $E = Pt$, where V_{min} and V_{max} represent the lower and upper limits of the voltage window at different current densities, i is the discharge current, m is the total weight of the cathode and anode, and t is the discharge time. The energy density of the ZIC can reach to 98.6 Wh kg^{-1} at the power density of 77.5 W kg^{-1}, even the power density of the ZIC is as high as 2480.6 W kg^{-1}, and the energy density still retains a high value of 29.7 Wh kg^{-1} (Fig. 4e). The energy and power densities of the ZIC are comparable to those of lithium-ion and sodium-ion capacitors [43–52]. Figure 4f shows the Nyquist plot of the ZIC, and the inset shows the fitted circuit diagram. The equivalent series resistance (ESR) represented by the intercept of semicircle on the real axis (in high-frequency regions) contains the contact resistance between the electrode material and electrolyte, and the internal resistance of the electrode material and electrolyte. The charge transfer resistance (R_{ct}) affected by the reaction kinetics is reflected by the radius of the semicircle. In low-frequency regions, the slope of the line represents the diffusion resistance of Zn ions in the electrolyte [53]. The ESR and R_{ct} of the ZIC are as low as 32.5 and 19.6 Ω, respectively, which implies the fast charge–discharge rate of the ZIC. The cycle life of the ZIC was investigated by GCD. Figure 4g shows the GCD curves of the initial and last ten cycles. As seen in Fig. 4h, after 15,000 GCD cycles at a current density of 5.224 A g^{-1}, the capacitance retention of the ZIC is as high as 83.6%, and the Coulombic efficiency is still above 93.3% during cycling. These above results exhaustively demonstrate the excellent performance of the ZIC. To demonstrate the excellent cycle stability of the ZIC, the posttest characterization of the MnO_2–CNTs cathode and MXene anode was conducted. As shown in Fig. S5a–d, the morphologies and structures after 15,000 GCD cycles have no obvious change, which indicates the excellent stability of the cathode and anode during cycling.

To illustrate the practical application of the ZIC, the aqueous gel electrolyte was used, and the corresponding electrochemical performance and flexibility were investigated.
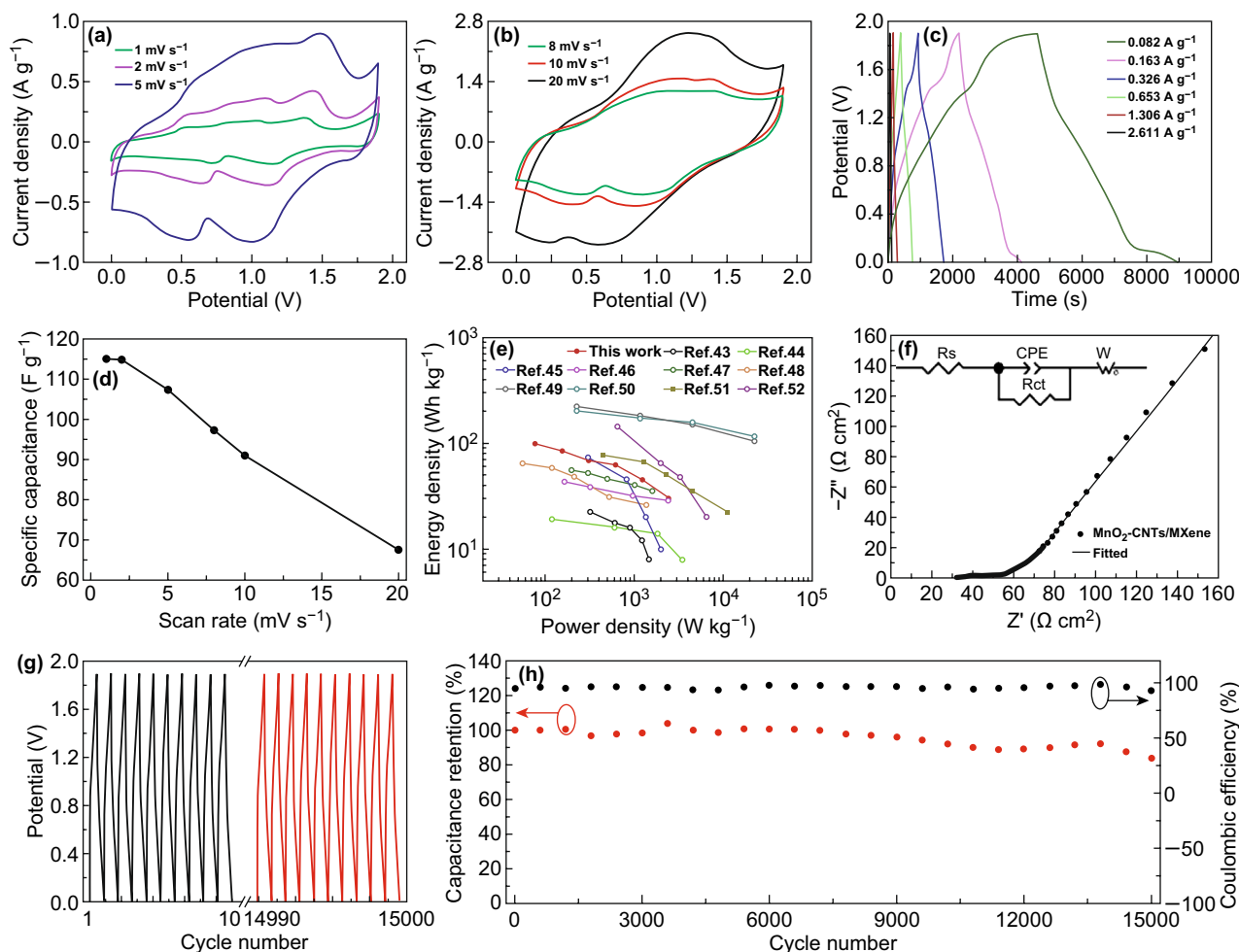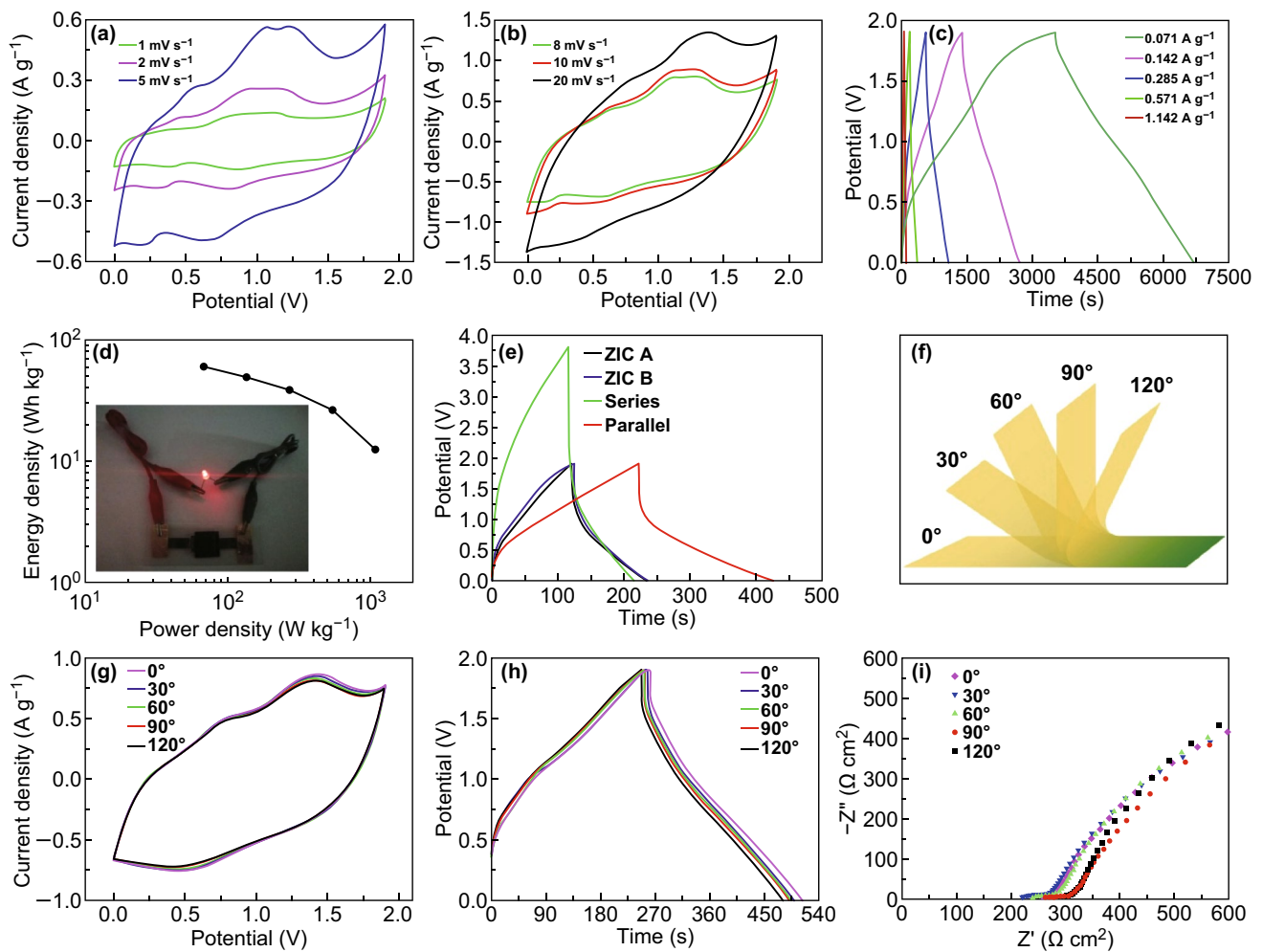
Fig. 4 Electrochemical performance of the ZIC in the aqueous liquid electrolyte. **a**, **b** CV curves with various scan rates, **c** GCD curves with various current densities, **d** specific capacitance versus scan rate, **e** energy and power density plot, **f** Nyquist plot (inset is a fitted circuit diagram), **g** GCD curves of the first and last ten cycles, and **h** cycle life and Coulombic efficiency of the ZIC

As shown in Fig. 5a, b, the CV curves of the ZIC also show the high current density and large enclosed area. In Fig. 5c, from the GCD curves of the ZIC, good linear potential–time profiles and long discharge times under certain current densities can be observed. The specific capacitance of the ZIC in an aqueous gel electrolyte is as high as 97.3 F g^{-1} at the scan rate of 1 mV s^{-1} (Fig. S6). Compared with the aqueous liquid electrolyte, owing to the lower conductivity of the aqueous gel electrolyte, the rate capability of the ZIC in the gel electrolyte is slightly worse than that in the liquid electrolyte. The energy and power densities of the ZIC in the aqueous gel electrolyte (Fig. 5d) also exhibit the high values of 67.8 Wh kg^{-1} (59.9 W kg^{-1}) and 1085.3 W kg^{-1} (12.4 Wh kg^{-1}), respectively. As shown in Fig. 5d inset, a

single ZIC can light up a LED brightly. To meet the energy and power needs, two ZICs were assembled in series and in parallel. Figure 5e presents the GCD curves of a single ZIC and ZICs connected in series and in parallel. Two ZICs connected in series exhibit a 3.8 V voltage window with similar discharge times. When the two ZICs are connected in parallel, their discharge time doubles compared to that of a single ZIC. These results obey the basic rule of series and parallel connections of capacitors. Figure 5f illustrates the schematic diagram of the flexible display of the ZIC in the aqueous gel electrolyte. The CV and GCD curves of the ZIC with bending angle from 0° to 120° are shown in Fig. 5g, h. It can be concluded that the specific capacitance of ZIC changes little during bending. (The capacitance retention calculated

Fig. 5 Electrochemical performance and flexibility of the ZIC in the aqueous gel electrolyte. **a, b** CV curves, **c** GCD curves, and **d** energy and power density plot (inset shows a LED drove brightly by a single ZIC) of the ZIC. **e** GCD curves of a single ZIC (A, B) and ZICs connected in series and in parallel. **f** Schematic diagram of the flexible display of the ZIC. **g** CV curves at a scan rate of 10 mV s^{-1}, **h** GCD curves at a current density of 0.415 A g^{-1}, and **i** Nyquist plot of the ZIC bent from 0° to 150°

by CV results remains almost 94.6% when bends up to 120° (Fig. S7).) The Nyquist plots of the flexible ZIC keep almost identical during bending except for a slight increase in ESR (increased from 218.7 Ω (0°) to 269.9 Ω (120°)), as shown in Fig. 5i. The above results imply that the designed ZIC in the aqueous gel electrolyte possesses excellent electrochemical performance and flexibility.

4 Conclusions

A new ZIC was successfully prepared by assembling free-standing MnO$_2$–CNTs battery-type cathode and MXene capacitor-type anode in aqueous liquid or aqueous gel electrolytes. The ZIC assembled in the aqueous electrolyte avoids the inflammable, volatile, and toxic safety issues. Similar to the lithium-ion and sodium-ion capacitors, the ZIC stores energy using the battery-type and capacitor-type energy storage mechanisms. As free-standing electrodes without the binder are adopted, the mass and volume of the ZIC are considerably lower. These above-mentioned reasons indicate the excellent energy storage performance of the ZIC. As expected, the ZIC exhibits a high specific capacitance of 115.1 F g^{-1} (scan rate of 1 mV s^{-1}), a high energy density of 98.6 Wh kg^{-1} (power density of 77.5 W kg^{-1}), and a high power density of 2480.6 W kg^{-1} (energy density of 29.7 Wh kg^{-1}). Even

after 15,000 GCD cycles, the ZIC exhibits a high capacitance retention of ~ 83.6% of its initial capacitance, and during the cycles, it has a high Coulombic efficiency of above 93.3%. In aqueous gel electrolyte, the ZIC also exhibits excellent performance. This study provides an effective way to design an ion capacitor with high energy and power densities, excellent cycle stability, long life, and high safety for the next-generation energy storage devices.

Electronic supplementary material The online version of this article (https://doi.org/10.1007/s40820-019-0301-1) contains supplementary material, which is available to authorized users.

References

1. M.S. Dresselhaus, I.L. Thomas, Alternative energy technologies. Nature **414**(6861), 332–337 (2001). https://doi.org/10.1038/35104599

2. D. Chao, C. Zhu, X. Xia, J. Liu, X. Zhang et al., Graphene quantum dots coated VO_2 arrays for highly durable electrodes for Li and Na ion batteries. Nano Lett. **15**(1), 565–573 (2015). https://doi.org/10.1021/nl504038s

3. M. Chen, D. Chao, J. Liu, J. Yan, B. Zhang, Y. Huang, J. Lin, Z.X. Shen, Rapid pseudocapacitive sodium-ion response induced by 2D ultrathin tin monoxide nanoarrays. Adv. Funct. Mater. **27**(12), 1606232 (2017). https://doi.org/10.1002/adfm.201606232

4. Z. Liu, H. Li, M. Zhu, Y. Huang, Z. Tang et al., Towards wearable electronic devices: a quasi-solid-state aqueous lithium-ion battery with outstanding stability, flexibility, safety and breathability. Nano Energy **44**, 164–173 (2018). https://doi.org/10.1016/j.nanoen.2017.12.006

5. J. Duay, M. Keny, T.N. Lambert, Evaluation of a ceramic separator for use in rechargeable alkaline Zn/MnO_2 batteries. J. Power Sources **395**, 430–438 (2018). https://doi.org/10.1016/j.jpowsour.2018.05.072

6. D. Zhao, Y. Wang, Y. Zhang, High-performance Li-ion batteries and supercapacitors based on prospective 1-D nanomaterials. Nano-Micro Lett. **3**(1), 62–71 (2011). https://doi.org/10.1007/bf03353653

7. J. Zhou, J. Yu, L. Shi, Z. Wang, H. Liu, B. Yang, C. Li, C. Zhu, J. Xu, A conductive and highly deformable all-pseudo-capacitive composite paper as supercapacitor electrode with improved areal and volumetric capacitance. Small **14**(51), 1803786 (2018). https://doi.org/10.1002/smll.201803786

8. A. Elmouwahidi, E. Bailon-Garcia, A.F. Perez-Cadenas, N. Fernandez-Saez, F. Carrasco-Marin, Development of vanadium-coated carbon microspheres: electrochemical behavior as electrodes for supercapacitors. Adv. Funct. Mater. **28**(35), 1802337 (2018). https://doi.org/10.1002/adfm.201802337

9. X. Liu, D. Li, X. Chen, W.-Y. Lai, W. Huang, Highly transparent and flexible all-solid-state supercapacitors based on ultralong silver nanowire conductive networks. ACS Appl. Mater. Interfaces **10**(38), 32536–32542 (2018). https://doi.org/10.1021/acsami.8b10138

10. Q. Zhang, J. Zhang, Z. Zhou, L. Wei, Y. Yao, Flexible quasi-solid-state 2.4 V aqueous asymmetric microsupercapacitors with ultrahigh energy density. J. Mater. Chem. A **6**(41), 20145–20151 (2018). https://doi.org/10.1039/c8ta07727d

11. H. Huang, D. Kundu, R. Yan, E. Tervoort, X. Chen, L. Pan, M. Oschatz, M. Antonietti, M. Niederberger, Fast Na-ion intercalation in zinc vanadate for high-performance Na-ion hybrid capacitor. Adv. Energy Mater. **8**(35), 1802800 (2018). https://doi.org/10.1002/aenm.201802800

12. N. Kurra, M. Alhabeb, K. Maleski, C.-H. Wang, H.N. Alshareef, Y. Gogotsi, Bistacked titanium carbide (MXene) anodes for hybrid sodium-ion capacitors. ACS Energy Lett. **3**(9), 2094–2100 (2018). https://doi.org/10.1002/aenm.201802800

13. J. Ding, W. Hu, E. Paek, D. Mitlin, Review of hybrid ion capacitors: from aqueous to lithium to sodium. Chem. Rev. **118**(14), 6457–6498 (2018). https://doi.org/10.1021/acs.chemrev.8b00116

14. P. Han, G. Xu, X. Han, J. Zhao, X. Zhou, G. Cui, Lithium ion capacitors in organic electrolyte system: scientific problems, material development, and key technologies. Adv. Energy Mater. **8**(26), 1801243 (2018). https://doi.org/10.1002/aenm.201801243

15. W. Zuo, R. Li, C. Zhou, Y. Li, J. Xia, J. Liu, Battery-supercapacitor hybrid devices: recent progress and future prospects. Adv. Sci. **4**(7), 1600539 (2017). https://doi.org/10.1002/advs.201600539

16. J. Xu, Z. Liao, J. Zhang, B. Gao, P.K. Chu, K. Huo, Heterogeneous phosphorus-doped WO_{3-x}/nitrogen-doped carbon nanowires with high rate and long life for advanced lithium-ion capacitors. J. Mater. Chem. A **6**(16), 6916–6921 (2018). https://doi.org/10.1039/c8ta00639c

17. J. Luo, W. Zhang, H. Yuan, C. Jin, L. Zhang et al., Pillared structure design of MXene with ultralarge interlayer spacing for high-performance lithium-ion capacitors. ASC Nano **11**(3), 2459–2469 (2017). https://doi.org/10.1021/acsnano.6b07668

18. Q. Yang, S. Cui, Y. Ge, Z. Tang, Z. Liu et al., Porous single-crystal $NaTi_2(PO_4)_3$ via liquid transformation of TiO_2 nanosheets for flexible aqueous Na-ion capacitor. Nano Energy **50**, 623–631 (2018). https://doi.org/10.1016/j.nanoen.2018.06.017

19. Y. Yang, Y. Tang, G. Fang, L. Shan, J. Guo et al., Li+ intercalated V2O5 nH2O with enlarged layer spacing and fast ion diffusion as an aqueous zinc-ion battery cathode. Energy Environ. Sci. **11**(11), 3157–3162 (2018). https://doi.org/10.1039/c8ee01651h

20. Z. Wang, F. Mo, L. Ma, Q. Yang, G. Liang et al., Highly compressible cross-linked polyacrylamide hydrogel-enabled compressible $Zn-MnO_2$ battery and a flexible battery-sensor system. ACS Appl. Mater. Interfaces **10**(51), 44527–44534 (2018). https://doi.org/10.1021/acsami.8b17607

21. B. Wu, G. Zhang, M. Yan, T. Xiong, P. He, L. He, X. Xu, L. Mai, Graphene scroll-coated alpha-MnO_2 nanowires as high-performance cathode materials for aqueous Zn-ion battery. Small **14**(13), 1703850 (2018). https://doi.org/10.1002/smll.201703850

22. M. Yan, P. He, Y. Chen, S. Wang, Q. Wei et al., Water-lubricated intercalation in V2O5 nH2O for high-capacity and high-rate aqueous rechargeable zinc batteries. Adv. Mater. **30**(1), 1703725 (2018). https://doi.org/10.1002/adma.201703725

23. A. Konarov, N. Voronina, J.H. Jo, Z. Bakenov, Y.-K. Sun, S.-T. Myung, Present and future perspective on electrode materials for rechargeable zinc-ion batteries. ACS Energy Lett. **3**(10), 2620–2640 (2018). https://doi.org/10.1021/acsenergylett.8b01552

24. G. Fang, J. Zhou, A. Pan, S. Liang, Recent advances in aqueous zinc-ion batteries. ACS Energy Lett. **3**(10), 2480–2501 (2018). https://doi.org/10.1021/acsenergylett.8b01426

25. J.-G. Wang, Z. Zhang, X. Zhang, X. Yin, X. Li, X. Liu, F. Kang, B. Wei, Cation exchange formation of prussian blue analogue submicroboxes for high-performance Na-ion hybrid supercapacitors. Nano Energy **39**, 647–653 (2017). https://doi.org/10.1016/j.nanoen.2017.07.055

26. B. Li, F. Dai, Q. Xiao, L. Yang, J. Shen, C. Zhang, M. Cai, Nitrogen-doped activated carbon for a high energy hybrid supercapacitor. Energy Environ. Sci. **9**(1), 102–106 (2016). https://doi.org/10.1039/c5ee03149d

27. B. Anasori, M.R. Lukatskaya, Y. Gogotsi, 2D metal carbides and nitrides (MXenes) for energy storage. Nat. Rev. Mater. **2**(2), 16098 (2017). https://doi.org/10.1038/natrevmats.2016.98

28. J. Zhou, J. Yu, L. Shi, Z. Wang, H. Liu, B. Yang, C. Li, C. Zhu, J. Xu, A conductive and highly deformable all-pseudocapacitive composite paper as supercapacitor electrode with improved areal and volumetric capacitance. Small **14**(51), 1803786 (2018). https://doi.org/10.1002/smll.201803786

29. C. Yang, Y. Tang, Y. Tian, Y. Luo, M.F.U. Din, X. Yin, W. Que, Flexible nitrogen-doped 2D titanium carbides (MXene) films constructed by an ex situ solvothermal method with extraordinary volumetric capacitance. Adv. Energy Mater.

8(31), 1802087 (2018). https://doi.org/10.1002/aenm.201802087

30. J. Tao, N. Liu, J. Rao, L. Ding, M.R. Al Bahrani, L. Li, J. Su, Y. Gao, Series asymmetric supercapacitors based on freestanding inner-connection electrodes for high energy density and high output voltage. Nanoscale **6**(24), 15073–15079 (2014). https://doi.org/10.1039/c4nr04819a

31. Y. Ma, Y. Yue, H. Zhang, F. Cheng, W. Zhao et al., 3D synergistical MXene/reduced graphene oxide aerogel for a piezoresistive sensor. ACS Nano **12**(4), 3209–3216 (2018). https://doi.org/10.1021/acsnano.7b06909

32. Y. Yue, N. Liu, W. Liu, M. Li, Y. Ma et al., 3D hybrid porous MXene-sponge network and its application in piezoresistive sensor. Nano Energy **50**, 79–87 (2018). https://doi.org/10.1016/j.nanoen.2018.05.020

33. S. Wang, N. Liu, C. Yang, W. Liu, J. Su et al., Fully screen printed highly conductive electrodes on various flexible substrates for asymmetric supercapacitors. RSC Adv. **5**(104), 85799–85805 (2015). https://doi.org/10.1039/c5ra16724h

34. Y. Yue, N. Liu, Y. Ma, S. Wang, W. Liu et al., Highly self-healable 3D microsupercapacitor with MXene-graphene composite aerogel. ASC Nano **12**(5), 4224–4232 (2018). https://doi.org/10.1021/acsnano.7b07528

35. B. Lee, H.R. Lee, H. Kim, K.Y. Chung, B.W. Cho et al., Elucidating the intercalation mechanism of zinc ions into alpha-MnO_2 for rechargeable zinc batteries. Chem. Commun. **51**(45), 9265–9268 (2015). https://doi.org/10.1039/c5cc02585k

36. D. Chao, C. Zhu, M. Song, P. Liang, X. Zhang et al., A high-rate and stable quasi-solid-state zinc-ion battery with novel 2D layered zinc orthovanadate array. Adv. Mater. **30**(32), 1803181 (2018). https://doi.org/10.1002/adma.201803181

37. H. Pan, Y. Shao, P. Yan, Y. Cheng, K.S. Han et al., Reversible aqueous zinc/manganese oxide energy storage from conversion reactions. Nat. Energy **1**, 16039 (2016). https://doi.org/10.1038/nenergy.2016.39

38. N. Liu, W. Ma, J. Tao, X. Zhang, J. Su et al., Cable-type supercapacitors of three-dimensional cotton thread based multi-grade nanostructures for wearable energy storage. Adv. Mater. **25**(35), 4925–4931 (2013). https://doi.org/10.1002/adma.201301311

39. W. Guo, X. Yan, F. Hou, L. Wen, Y. Dai et al., Flexible and free-standing SiO_x/CNT composite films for high capacity and durable lithium ion batteries. Carbon **152**, 888–897 (2019). https://doi.org/10.1016/j.carbon.2019.06.088

40. P. He, M. Yan, G. Zhang, R. Sun, L. Chen, Q. An, L. Mai, Layered VS_2 nanosheet-based aqueous Zn ion battery cathode. Adv. Energy Mater. **7**(11), 1601920 (2017). https://doi.org/10.1002/aenm.201601920

41. S. Wang, N. Liu, J. Tao, C. Yang, W. Liu et al., Inkjet printing of conductive patterns and supercapacitors using a multi-walled carbon nanotube/Ag nanoparticle based ink. J. Mater. Chem. A **3**(5), 2407–2413 (2015). https://doi.org/10.1039/c4ta05625f

42. S. Wang, N. Liu, J. Rao, Y. Yue, K. Gao et al., Vertical finger-like asymmetric supercapacitors for enhanced performance at

high mass loading and inner integrated photodetecting systems. J. Mater. Chem. A **5**(42), 22199–22207 (2017). https://doi.org/10.1039/c7ta06306g

43. L. Li, S. Peng, H.B. Wu, L. Yu, S. Madhavi, X.W. Lou, A flexible quasi-solid-state asymmetric electrochemical capacitor based on hierarchical porous V_2O_5 nanosheets on carbon nanofibers. Adv. Energy Mater. **5**(17), 1500753 (2015). https://doi.org/10.1002/aenm.201500753

44. N. Arun, A. Jain, V. Aravindan, S. Jayaraman, W.C. Ling, M.P. Srinivasan, S. Madhavi, Nanostructured spinel $LiNi_{0.5}Mn_{1.5}O_4$ as new insertion anode for advanced Li-ion capacitors with high power capability. Nano Energy **12**, 69–75 (2015). https://doi.org/10.1016/j.nanoen.2014.12.006

45. F. Wang, C. Wang, Y. Zhao, Z. Liu, Z. Chang, L. Fu, Y. Zhu, Y. Wu, D. Zhao, A quasi-solid-state Li-ion capacitor based on porous TiO_2 hollow microspheres wrapped with graphene nanosheets. Small **12**(45), 6207–6213 (2016). https://doi.org/10.1002/smll.201602331

46. H. Li, Y. Zhu, S. Dong, L. Shen, Z. Chen et al., Self-assembled Nb_2O_5 nanosheets for high energy-high power sodium ion capacitors. Chem. Mater. **28**(16), 5753–5760 (2016). https://doi.org/10.1021/acs.chemmater.6b01988

47. S. Dong, L. Shen, H. Li, G. Pang, H. Dou et al., Flexible sodium-ion pseudocapacitors based on 3D $Na_2Ti_3O_7$ nanosheet arrays/carbon textiles anodes. Adv. Funct. Mater. **26**(21), 3703–3710 (2016). https://doi.org/10.1002/adfm.201600264

48. Z. Le, F. Liu, P. Nie, X. Li, X. Liu, Z. Bian, G. Chen, H.B. Wu, Y. Lu, Pseudocapacitive sodium storage in mesoporous single-crystal-like TiO_2-graphene nanocomposite enables high-performance sodium-ion capacitors. ACS Nano **11**(3), 2952–2960 (2017). https://doi.org/10.1021/acsnano.6b08332

49. Q. Xia, H. Yang, M. Wang, M. Yang, Q. Guo, L. Wan, H. Xia, Y. Yu, High energy and high power lithium-ion capacitors based on boron and nitrogen dual-doped 3D carbon nanofibers as both cathode and anode. Adv. Energy Mater. **7**(22), 1701336 (2017). https://doi.org/10.1002/aenm.201701336

50. F. Sun, X. Liu, H.B. Wu, L. Wang, J. Gao, H. Li, Y. Lu, In situ high-level nitrogen doping into carbon nanospheres and boosting of capacitive charge storage in both anode and cathode for a high-energy 4.5 V full-carbon lithium-ion capacitor. Nano Lett. **18**(6), 3368–3376 (2018). https://doi.org/10.1021/acs.nanolett.8b00134

51. S. Liu, J. Zhou, Z. Cai, G. Fang, Y. Cai, A. Pan, S. Liang, Nb_2O_5 quantum dots embedded in MOF derived nitrogen-doped porous carbon for advanced hybrid supercapacitor applications. J. Mater. Chem. A **4**(45), 17838–17847 (2016). https://doi.org/10.1039/c6ta07856g

52. M. Ulaganathan, V. Aravindan, W.C. Ling, Q. Yan, S. Madhavi, High energy Li-ion capacitors with conversion type Mn_3O_4 particulates anchored to few layer graphene as the negative electrode. J. Mater. Chem. A **4**(39), 15134–15139 (2016). https://doi.org/10.1039/c6ta05944a

53. R.B. Rakhi, W. Chen, D. Cha, H.N. Alshareef, Substrate dependent self-organization of mesoporous cobalt oxide nanowires with remarkable pseudocapacitance. Nano Lett. **12**(5), 2559–2567 (2012). https://doi.org/10.1021/nl300779a